**ADVANCED
MATERIALS
INTERFACES**

Supporting Information

Simultaneous Deconvolution of In-Plane and Out-of-Plane Forces of HOPG at the Atomic Scale under Ambient Conditions by Multifrequency Atomic Force Microscopy

Anna L. Eichhorn and Christian Dietz*

Supporting Information:

Simultaneous Deconvolution of In-plane and Out-of-plane Forces of HOPG at the Atomic Scale under Ambient Conditions by Multifrequency Atomic Force Microscopy

Anna L. Eichhorn and Christian Dietz*

Physics of Surfaces, Institute of Materials Science, Technische Universität Darmstadt,

Alarich-Weiss-Str. 2, 64287 Darmstadt, Germany

Email: eichhorn@pos.tu-darmstadt.de, dietz@pos.tu-darmstadt.de

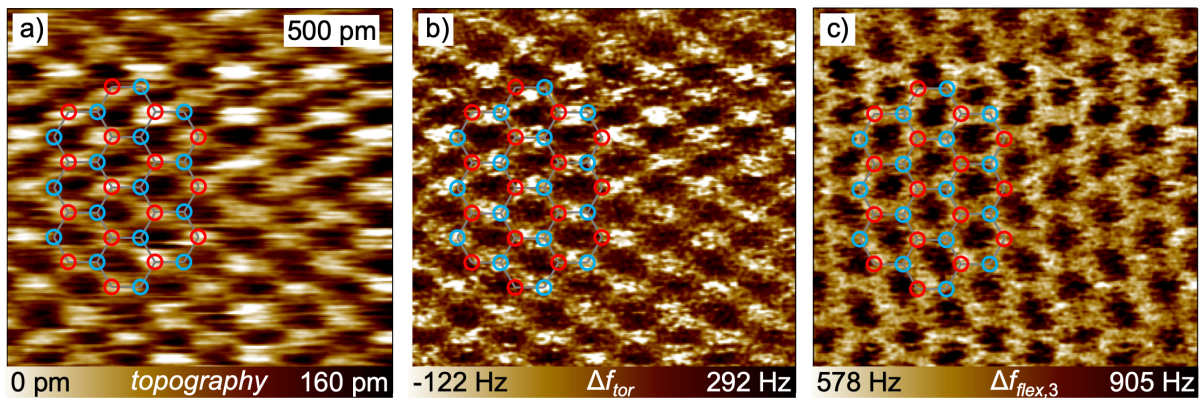**Inverted AFM images of HOPG taken in AMFlex2-FMTor1-FMFlex3 mode**

Figure S1. Inverted AFM images of HOPG taken in AMFlex2-FMTor1-FMFlex3 mode: a) topography image, and b) torsional and c) flexural frequency-shift images. Imaging parameters: $A_{0\,(flex,2)} = 770$ pm, $A_{flex,2} = 100$ pm, $A_{tor} = 80$ pm, $A_{flex,3} = 220$ pm.

Calibration of inverse optical lever sensitivities and oscillation amplitudes

The inverse optical lever sensitivity (InvOLS) was calibrated from the gradient of a curve of static deflection versus z-sensor position with a comparably low voltage setpoint to trigger, to protect the tip from wearing off. The calibration of the deflection has a major impact on the interpretation of the spectroscopy data because it is required for determining the actual tip–sample distance d. Consequently, calibrating the dynamic sensitivity from curves of amplitude versus tip–sample distance also depends on the accuracy of the static-deflection calibration.

That is why we determined the amplitude sensitivities from thermal-tune data based on the equipartition theorem.[1–3] Therefore, the flexural and lateral thermal noise spectra were collected and the observed power spectral densities (PSDs) were fitted by[4, 5]

$$\gamma_{flex} = \sqrt{\frac{2k_B T}{\pi k_{flex} f_{0,flex} P_{DC} Q_{flex}}}, \tag{1}$$

$$\gamma_{tor} = \sqrt{\frac{2k_B T}{\pi k_{tor} f_{0,tor} P_{DC} Q_{tor}}}, \tag{2}$$

where γ is the InvOLS, k_B is the Boltzmann constant, T is the absolute temperature, f_0 is the resonance frequency, P_{DC} is the PSD of the oscillator at DC, and Q is the quality factor. The flexural-force constants k_{flex} of the first two bending eigenmodes and the torsional torque constant k_{Φ} were determined by using the Sader method:[6, 7]

$$k_{flex} = 0.1906 \rho b^2 L Q_{flex} f_{0,flex}^2 \Gamma_i^{flex}(f_{flex}), \tag{3}$$

$$k_{\Phi} = 0.1592 \rho b^4 L Q_{tor} f_{0,tor}^2 \Gamma_i^{tor}(f_{tor}), \tag{4}$$

where ρ is the density of air, b is the width and L is the length of the cantilever, and Γ_i is the imaginary part of the hydrodynamic function. In the limit of small torsion angle, the torsional force constant can be calculated from the torsional torque constant by[8]

$$k_{tor} = \frac{k_{\Phi} L}{(L - \Delta L) h^2}, \tag{5}$$

where $L/(L-\Delta L)$ accounts for the influence of the tip set-back ΔL, and h is the tip height.

Note that γ_{tor} as determined from Equation (2) was around twice that estimated from imaging. It is well known that it is not straightforward to determine the torsional sensitivity, which is why we used the results of atomically resolved imaging for the calibration in the end. We observed that the torsional frequency shift at maximum counts of the image histograms decreased asymptotically with increasing torsional amplitude, and we assigned the beginning of the asymptotic value to amplitude values that were larger than half of the interatomic spacings. Consequently, the torsional sensitivity was estimated as being 11 nm/V. Currently to the best of our knowledge there is no method available that provides a higher accuracy for the calibration of the dynamic torsional invOLS. The improvement of the calibration methods for the dynamic torsional invOLS is of high importance for further research in this field.

Unfortunately, it was not possible to determine the third-flexural-eigenmode sensitivity and force constant from Equations (1) and (3) because of the small response of the resonance peak in the thermal spectrum. That is why we derived the values from the first- and second-eigenmode values. The force constant was calculated using the equation introduced by Labuda et al.[3] for flexural eigenmodes:

$$k_n = k_1 \left(\frac{f_n}{f_1} \right)^{\xi},$$

(6)

where the power-law exponent ξ can be determined from the known values for the second eigenmode as 1.76. The third-eigenmode sensitivity was estimated as being $\gamma_{flex,3} = 10$ nm/V from the second-eigenmode sensitivity using the relations introduced by Garcia et al.[9] for rectangular cantilevers.

Influence of cantilever mean deflection in AM-AFM using higher eigenmodes on atomic-scale imaging of HOPG

In general, it is not straightforward to assign the atomic positions from AFM images taken on HOPG. Several groups have shown that the appearance of the topographical contrast depends on whether imaging is accomplished in the attractive or repulsive regime, and the shown height image resembles a checkerboard pattern, which was also predicted and observed by other groups working in the field of AFM or scanning tunneling microscopy (STM).[10–12] In a theoretical study, Sasaki et al. showed that the contrast that can be observed on HOPG in the repulsive regime depends strongly on the configuration of the tip.[10] Besides the number and type of tip atoms involved in the imaging process, the tilt angle of the tip and the bond length and tip orientation relative to the surface were also predicted to influence the contrast of the height images. Another explanation for the appearance of the twofold symmetry was introduced by Wong et al. and Xu et al.[11–13] for STM images. They showed that the offset of the topmost carbon layer relative to the second one as well as the increased coupling between these layers can also result in a checkerboard pattern. Because of the observation that the topography images of HOPG showed a certain offset between trace and retrace, which depends on the scan velocity as well as the scan angle, in our setup we assume that the checkerboard pattern might originate from a tip-induced shift of the topmost carbon layer relative to the one beneath. Based on this assumption, it must be clarified how the first layer of carbon atoms can be lifted despite the fact that we observe exclusively repulsive phase and frequency-shift values in the second and third eigenmode channel, respectively. The solution to this puzzle was found by observing the mean deflection of the cantilever. In general, the cantilever deflection is assumed to play a minor role

in dynamic spectroscopy, which is especially the case for large amplitudes and stiff cantilevers. However, as shown by Kawai and coworkers[14] and recently in work by Yalcin *et al.*,[15] in particular at close tip–sample distances, the mean deflection of the cantilever cannot be neglected in dynamic spectroscopy. To understand better how the cantilever deflection influences the oscillation behavior, we obtained curves of mean deflection versus tip–sample distance including first-, second-, and third-eigenmode excitation, and simultaneously we recorded the deflection values while triggering at an amplitude value that was ~10% of the free second flexural amplitude. Additionally, we measured static deflection versus tip–sample distance (no dynamic drive) with the same cantilever. As shown in Figure S2a, the tip–sample distance d was calculated from the z-sensor position minus the tip height h plus the mean deflection as known from static spectroscopy, where the deflection is defined as negative for attractive and positive for repulsive long-range tip–sample interaction. The results of the curves of (mean) deflection versus tip–sample distance are shown in Figure S2b.
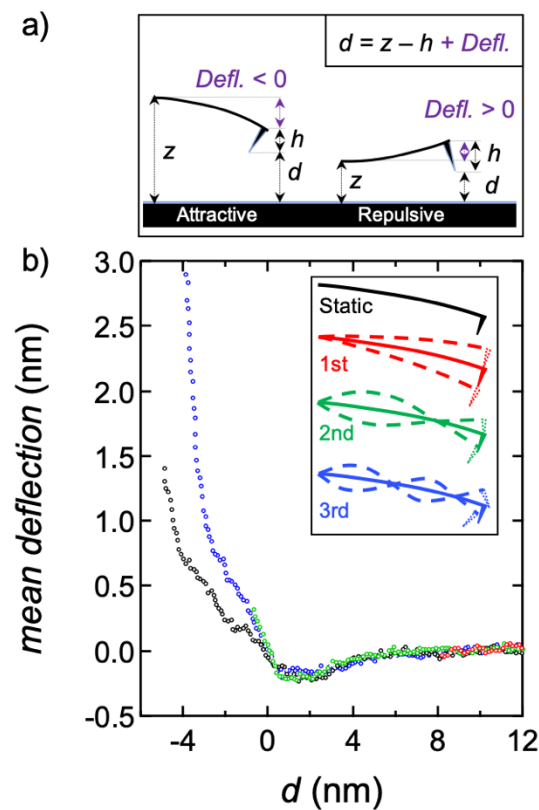

Figure S2. Comparison of mean deflection for different eigenmode oscillations as well as the static case on HOPG upon approach. a) Scheme for determining tip–sample distance from z-sensor position, tip height, and mean deflection (purple). b) Plot of mean deflection vs. tip–sample distance for static case (black), first flexural eigenmode (red), second flexural eigenmode (green), and third flexural eigenmode (blue).

4

Interestingly, the curves of mean deflection versus tip–sample distance show the same overall trend for all three dynamic modes and strongly resemble the trend of the curve of static deflection versus distance (up to $d = -1$ nm). Furthermore, it becomes evident that with higher eigenmodes, significantly higher mean deflections can be reached at similar amplitude setpoint ratios, which is a consequence of the enhanced dynamic stiffness. The curve of mean deflection versus tip–sample distance for the first-eigenmode oscillation additionally explains why we could not show atomic resolution: the smallest tip–sample distance achievable was still ~8 nm. Consequently, this observation corroborates the general assumption that the mean cantilever deflection can be neglected for the standard tapping mode with the first-eigenmode oscillation. However, we strongly recommend analyzing the mean-deflection behavior when using higher-eigenmode oscillations for feedback operation for a reliable interpretation of the obtained images.

Hysteretic behavior in spectroscopic experiments

Because we noticed an unexpectedly high hysteresis between the approach and retract curves of the (mean) deflection versus tip–sample distance, to clarify the origin of the hysteresis we made additional static-deflection measurements with the same tip on freshly cleaved HOPG and silicon stored under ambient conditions. The resulting plots as well as a schematic of the possible scenarios on the two different materials close to the surface are shown in Figure S3.
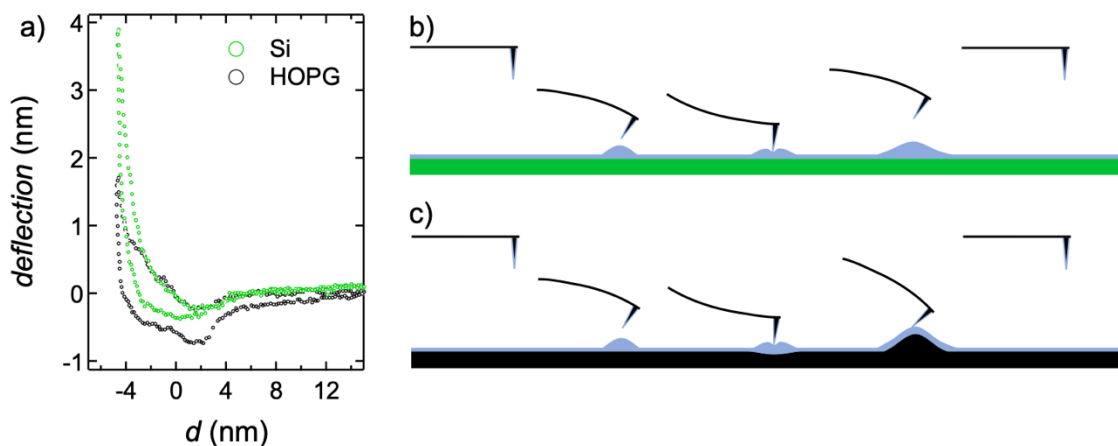

Figure S3. Comparison of hysteretic behavior upon approach and retract for silicon and HOPG with a DLC AFM tip. a) Deflection vs. tip–sample distance on silicon (green) and HOPG (black). b) and c) Scheme of tip–sample interactions on silicon and HOPG, respectively.

Usually, hysteretic behavior is observed for viscous materials such as polymers and biological cells because of the indentation of the stiff cantilever into the softer material, which causes plastic deformation, dissipation within the material, and strong attractive forces between tip and sample. On stiff and hydrophobic substrates such as HOPG and silicon, we expect neither a strong indentation nor a strong attractive tip–sample interaction or dissipation in general. However, the very close proximity of the tip to the sample means that van der Waals attraction and capillary interaction of water layers, which are present at both tip and sample under ambient conditions, cannot be neglected and are most likely responsible for the hysteresis. However, the question arises as to where the difference between the retract curves taken on silicon and on HOPG comes from. Figure S3a shows that the approach behavior of the DLC-coated tip to the silicon and the HOPG surface is very similar, and this behavior can be explained by the similar water wettability of the substrates. Both freshly cleaved HOPG and silicon stored under ambient conditions were shown to have a water contact angle of ~60°.[16, 17] However, the Hamaker constant between silicon and carbon is approximately half of that for HOPG.[18] This information matches the observation of stronger hysteresis on HOPG. Figure S3b and c show schematically the different interaction scenarios on silicon and HOPG. During approach, we assume that capillary interaction forces dominate the deflection of the cantilever on both substrates, whereas we assume an additional effect of a strong van der Waals adhesion on HOPG. This can lead to a local lift of the topmost carbon layer during retraction of the cantilever.[19] Consequently, this effect is also very likely to occur during imaging, which might have caused the contrast inversion of the images shown in the main text.

Comparison of topography, mean-deflection, and third-eigenmode frequency-shift images and cross sections for different third-flexural-eigenmode amplitudes

Figure S4 shows the topography (left) and third-eigenmode frequency-shift images (right) taken with three different values of $A_{flex,3}$. Additionally, the cross sections along the pink line marked in all the images can be seen in the center, while also plotted are the cross sections through the mean-deflection images (not shown). By comparing the results, it becomes apparent that the mean deflection compensates for a large amount of the height signal, as mentioned in the main text. This explains why we see such a high corrugation amplitude in the topography images. Second, we see from Figure S4b, e, and h that the minimum in the frequency shift always appears at the bond and the maximum at the hollow side. This is also the case for the height signal in Figure S4h where $A_{flex,3} = 509\,\text{pm}$. In contrast, for $A_{flex,3} = 364\,\text{pm}$, the minimum in height appears at the hollow side and the maximum at the bonds, which means that

the contrast is inverted. For $A_{flex,3}$ = 436 pm, the height signal has its inflection points at the positions of the carbon bonds and the hollow sides, resulting in a shifted appearance of both images. We assume that the different contrast relations originate from the different distances relative to the surface while imaging, which result from the variation of the third-eigenmode amplitude.
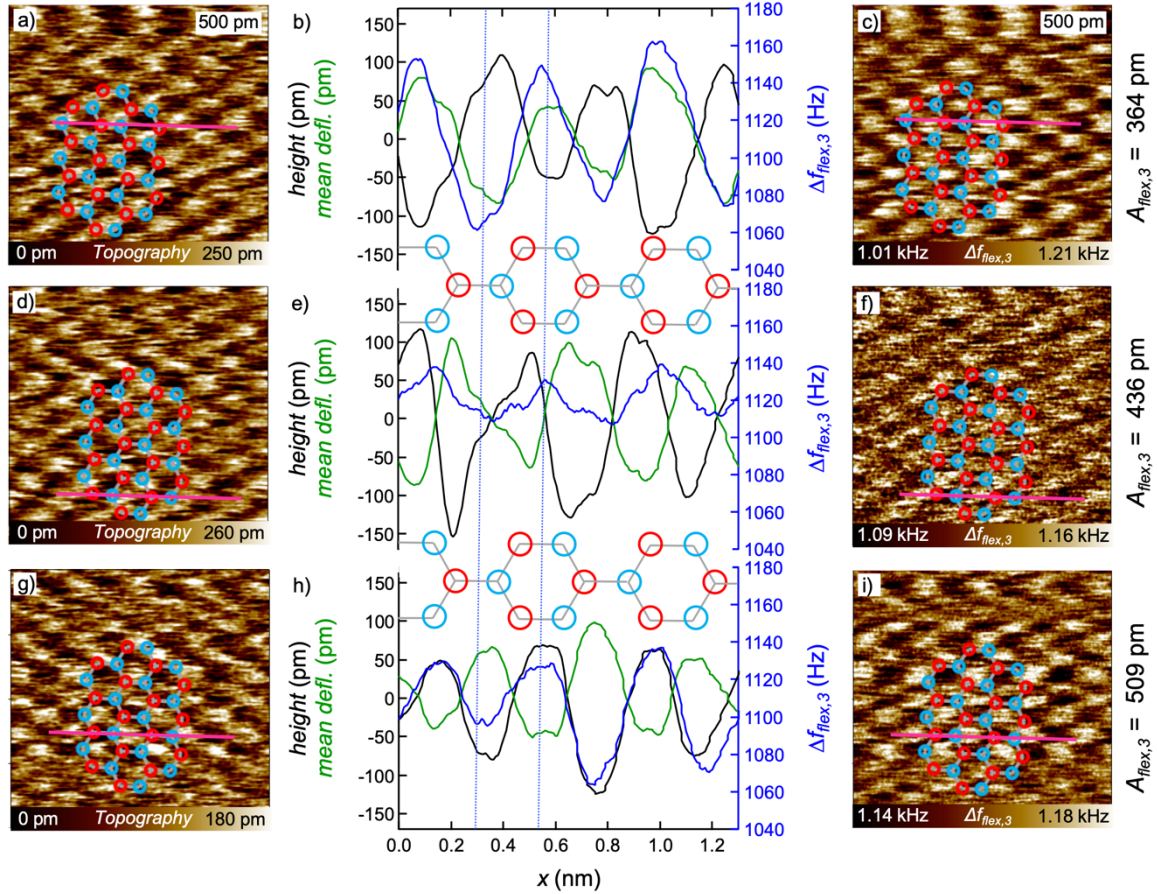

Figure S4. Comparison of topography, mean-deflection, and third-eigenmode frequency-shift images and cross sections for three different third-flexural-eigenmode amplitude setpoints. a), d), g) Topography images, b), e), h) cross sections drawn along the pink lines, and c), f), i) third-eigenmode frequency-shift images at $A_{flex,3}$ = 364 pm (a–c), $A_{flex,3}$ = 436 pm (d–f), and $A_{flex,3}$ = 509 pm (g–h). Further imaging parameters: $A_{flex,2}$ = 68 pm, A_{tor} = 0 pm.

Calculation of forces from spectroscopic data

The out-of-plane ($F_{flex,3}$) and in-plane (F_{tor}) forces were calculated from the frequency-shift data based on the approach of Sader and Jarvis.[20] The modified formulas for the multimodal approach used in this study, which can be implemented in a MATLAB code, are

$$F_{flex,3}(d) = \frac{2k_{flex,3}}{f_{0\,(flex,3)}} \int_d^\infty \left(1 + \frac{\sqrt{A_{flex,2} + A_{0\,(flex,3)}}}{8\sqrt{\pi(x-d)}}\right) \Delta f_{flex,3}(x) - \frac{\sqrt{(A_{flex,2} + A_{0\,(flex,3)})^3}}{\sqrt{2(x-d)}} \frac{d\Delta f_{flex,3}(x)}{dx} dx, \quad (7)$$

$$F_{tor}(d) = -\frac{2k_{tor}}{f_{0\,(tor)}} \int_d^\infty \left(1 - \sqrt{2(A_{flex,2} + A_{0\,(flex,3)})}\right) \frac{\Delta f_{flex,3}(x)}{\sqrt{(x-d)}} dx, \quad (8)$$

where $k_{flex,3}$ (resp. k_{tor}) is the third flexural (first torsional) eigenmode stiffness, $A_{flex,2}$ is the tip–sample-distance-dependent amplitude of the second flexural eigenmode, $A_{0\,(flex,3)}$ is the amplitude setpoint of the third flexural eigenmode, and $\Delta f_{flex,3}$ (resp. Δf_{tor}) and $f_{0\,(flex,3)}$ (resp. $f_{0\,(tor)}$) are the frequency shift and resonance frequency, respectively, of the third flexural (first torsional) eigenmode.

Influence of second-flexural-eigenmode amplitude-setpoint on torsional and third-flexural frequency shifts.

Figure S5 shows the histograms resulting from atomically resolved (a) third-eigenmode and (b) torsional frequency-shift images of HOPG for varying second-eigenmode amplitude setpoints. In Figure S5c, the frequency shifts at maximum counts are plotted as a function of the second-flexural-eigenmode amplitude setpoint. Additionally, the frequency shifts at FWHM of the histograms in Figure S5a and b are shown with dotted lines. From Figure S5c, it becomes evident that the third-eigenmode frequency-shift images are much more influenced by the second-flexural-eigenmode amplitude setpoint compared to the torsional frequency-shift images.
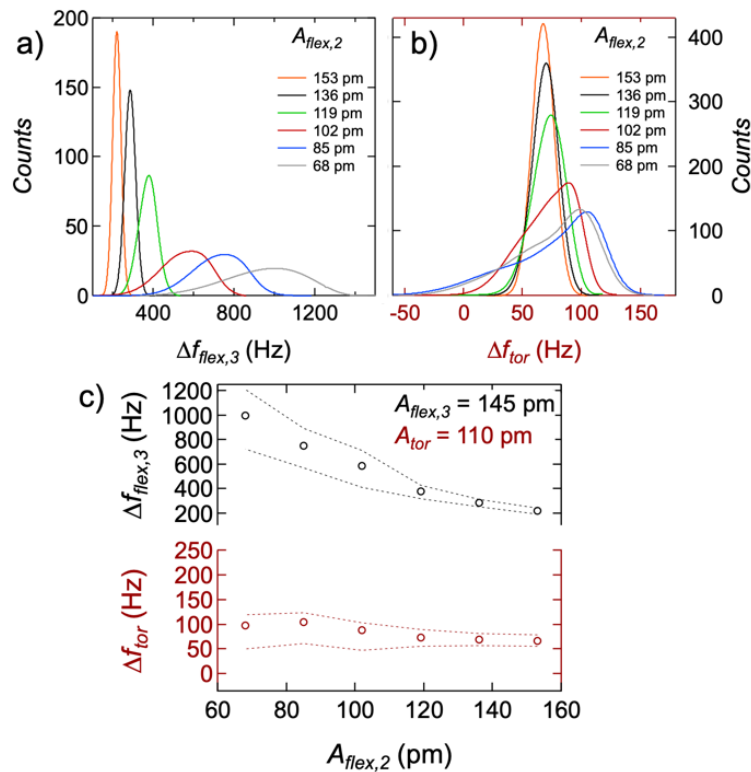

Figure S5. Influence of second-eigenmode flexural-oscillation amplitude setpoint on the observed frequency shifts. Histograms of a) third-eigenmode flexural and b) torsional frequency-shift images for different second-eigenmode flexural-amplitude setpoints. Third-eigenmode flexural and torsional frequency shifts at maximum counts (open circles) and at FWHM (dotted lines) as a function of the second-flexural-eigenmode amplitude setpoint at a constant torsional-eigenmode amplitude of 110 pm and a constant flexural-eigenmode amplitude of 145 pm.

Calculation of forces from frequency-shift images using Fourier method for higher eigenmodes

We modified the Fourier method to reconstruct the forces in the z-direction from the flexural frequency shift of the higher eigenmodes. The formula for the frequency shift as a function of the force for the second eigenmode was introduced by Herruzo et al.[21] based on the work of Giessibl et al.[22]. Kawai and coworkers showed that the relation between frequency shift and forces is also valid for higher flexural as well as for torsional eigenmodes:[23]

$$\Delta f_i(x) = -\frac{f_i}{2\pi k_i} \int_{-A_{sp}}^{A_{sp}} F'_{ts}(x+q) \frac{1}{\sqrt{A_{sp}^2 - q^2}} dq, \tag{9}$$

where Δf_i is the frequency shift, f_i is the resonance frequency, and k_i is the force constant of the ith eigenmode. A_{sp} is the setpoint amplitude of the oscillation used for the topographical feedback, and F'_{ts} is the first derivative of the force.

Introducing the variable $q = A_{sp}\cos\left(\omega t - \frac{\pi}{2}\right)$ allows the convolution of the force gradient with the semicircle $\frac{2A_{sp}^2}{\pi}\sqrt{A_{sp}^2 - q^2}$ [21, 22].

Equivalently to Seeholzer et al., we used the exact formula for Δf_i:[22, 24, 25]

$$\Delta f_i(x) = \frac{f_i}{2k_i}\langle k_{ts}\rangle(x), \tag{10}$$

where $<k_{ts}>$ is the weight force gradient. The first derivative of the tip–sample force, F'_{ts}, can be expressed as

$$F'_{ts}(x+q) = -k_{ts}(x+q). \tag{11}$$

From Equations (9–11), it follows that

$$\langle k_{ts}\rangle(x) = \frac{1}{\pi} \int_{-A_{sp}}^{A_{sp}} k_{ts}(x+q) \frac{1}{\sqrt{A_{sp}^2 - q^2}} dq. \tag{12}$$

The tip–sample stiffness k_{ts} can be determined from the second derivative of the tip–sample energy E_{ts} expressed by a Fourier series with the components a_n and b_n:

$$k_{ts}(x) = \sum_{n=1}^{N} -a_n \left(\frac{2\pi n}{L}\right)^2 \sin\left(\frac{2\pi n}{L}x\right) - b_n \left(\frac{2\pi n}{L}\right)^2 \cos\left(\frac{2\pi n}{L}x\right) = \frac{d^2 E_{ts}(x)}{dx^2}, \tag{13}$$

where L is the line length and N is the Nyquist frequency, which is half of the sampling rate s:

$$N = \frac{S}{2L}. \tag{14}$$

By substituting the formula for k_{ts} into that for $<k_{ts}>$, we obtain

$$\langle k_{ts} \rangle(x) = \sum_{n=1}^{N} -a_n \left(\frac{2\pi n}{L}\right)^2 \sin\left(\frac{2\pi n}{L}x\right) J_0\left(\frac{2\pi n A_1}{L}\right) - b_n \left(\frac{2\pi n}{L}\right)^2 \cos\left(\frac{2\pi n}{L}x\right) J_0\left(\frac{2\pi n A_1}{L}\right), \tag{15}$$

where J_0 is the Bessel function of the first kind and zero order. Assuming that the frequency-shift data of the line can be expressed as a Fourier series with the components α_n and β_n, i.e.,

$$\Delta f_i(x) = \sum_{n=1}^{N} \alpha_n \sin\left(\frac{2\pi n}{L}x\right) + \beta_n \cos\left(\frac{2\pi n}{L}x\right), \tag{16}$$

we can determine the expressions for a_n and b_n via direct comparison of the formulas. As in the work of Seeholzer *et al.*, the factors α_n and β_n were determined from the scalar projection of the data on the relevant sine or cosine function divided by a normalization factor:[25]

$$\alpha_n = \int \frac{2\Delta f_i(x)}{L} \sin\left(\frac{2\pi n}{L}x\right) dx, \tag{17}$$

$$\beta_n = \int \frac{2\Delta f_i(x)}{L} \cos\left(\frac{2\pi n}{L}x\right) dx. \tag{18}$$

This allows the determination of forces from frequency-shift data of higher eigenmodes, such as shown in the main text.

Comparison of original frequency-shift data with frequency-shift validation data along distinct cross sections

Figure S6 shows that the frequency-shift validation images determined with the Fourier method match the contrast of the original images. The main difference between the original and validation images is the frequency-shift offset, which results from the assumptions behind the Fourier method, as discussed in the main text. Additionally, the validation images appear much smoother than the original images, which is a consequence of the Fourier algorithm. To directly compare some distinct lines, we show the cross sections marked in the original and validation images in Figure S7. The positions of the cross sections are the same as those in the main text.
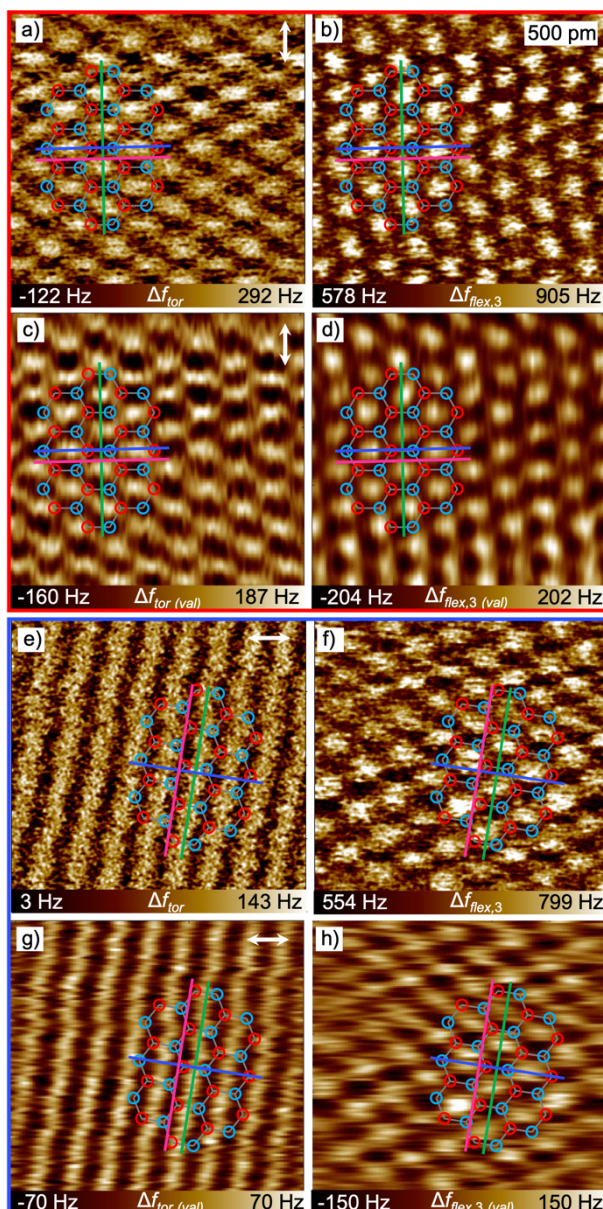
Figure S6. Original frequency-shift images (a, b, e, f) and frequency-shift validation images (c, d, g, h) determined by using the Fourier method. The torsional validation data (a, c, e, g) were calculated using the monomodal Fourier method, and the flexural validation data (b, d, f, h) were calculated using the bimodal Fourier method. Red: scan angle = 0°, A_{tor} = 80 pm, $A_{flex,2}$ = 100 pm, $A_{0\,(flex,2)}$ = 770 pm, $A_{flex,3}$ = 220 pm. Blue: scan angle = 90°, A_{tor} = 110 pm, $A_{flex,2}$ = 90 pm, $A_{0\,(flex,2)}$ = 770 pm, $A_{flex,3}$ = 150 pm.

Figure S7 shows that the frequency-shift validation images reproduce the original frequency-shift data nicely at the positions of the hollow sides and the carbon bonds, as seen in a, c, d, and f. Nevertheless, in Figure S7c the flexural frequency shift is not reproduced perfectly at the distinguishable atomic sides. For the pink cross sections in Figure S7b and e, the discrepancies between the validation and original frequency-shift data are slightly larger. This must be

considered when interpreting the force images, but the overall reproduction of the frequency-shift images is satisfying.
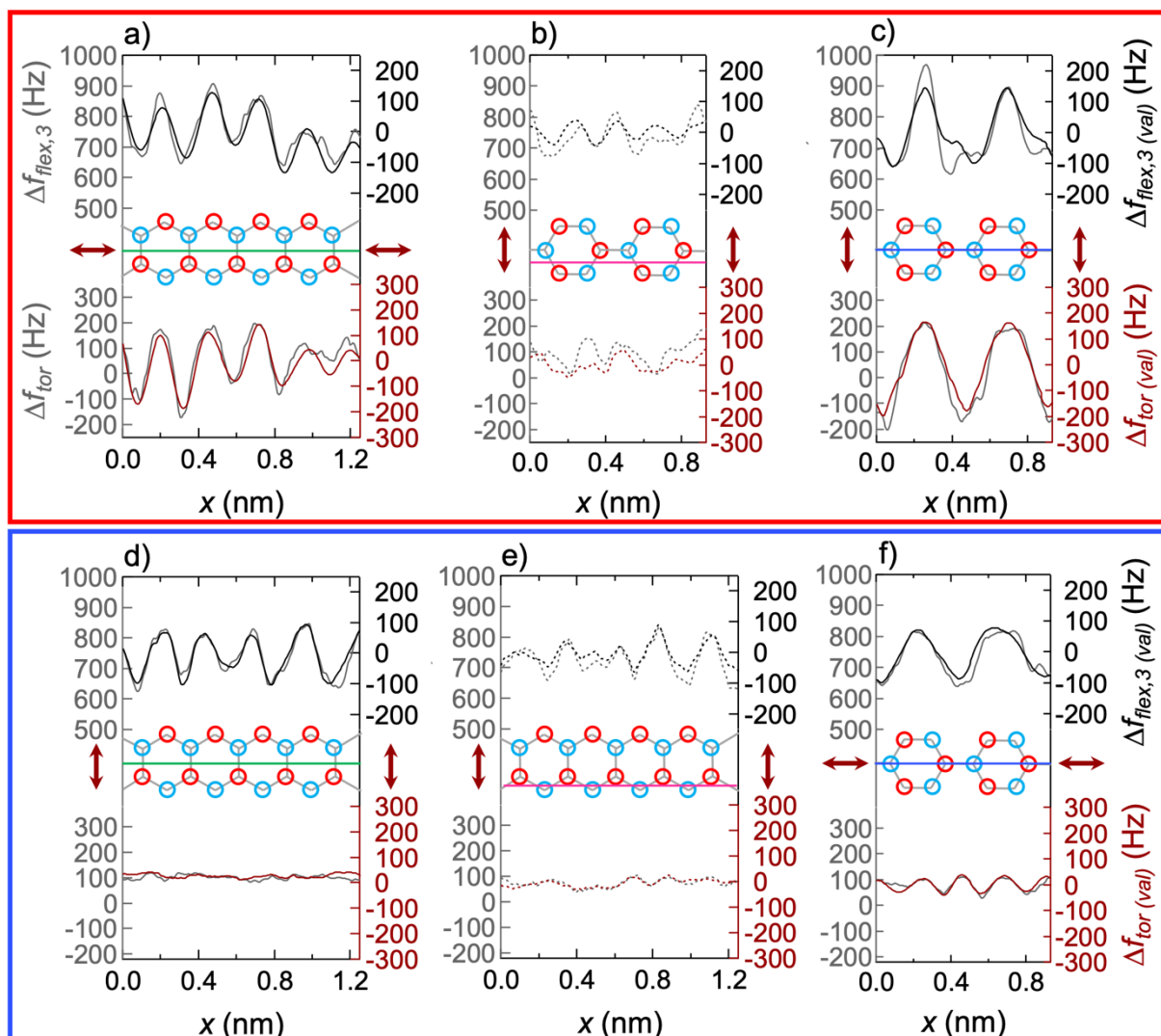

Figure S7. Cross-sectional profiles drawn through the original and validation frequency-shift images of HOPG along the pink, blue, and green lines in Figure S6. Profiles and axis labels are shown in gray for the original frequency-shift data, black for the flexural validation frequency-shift data, and red for the torsional validation frequency-shift data. The torsional oscillation was aligned approximately along the zigzag (resp. armchair) direction of the carbon hexagons for the cross sections shown in the red frame (a–c) (resp. blue frame (d–f)). The cross sections in a), d), and e) were drawn along the zigzag direction and in b), c), and e) along the armchair direction of the carbon hexagons. The a), d) green and c), f) blue marked cross sections cut the center of the hollow side, whereas the b), e) pink marked cross sections are offset from the center of the hollow side by the particular torsional amplitude values.

References

[1]   H. J. Butt, M. Jaschke, *Nanotechnology* **1995**, *6*, 1-7

[2]   J. L. Hutter, J. Bechhoefer, *Review of Scientific Instruments* **1993**, *64*, 1868-1873

[3]   A. Labuda, M. Kocun, M. Lysy, T. Walsh, J. Meinhold, T. Proksch, W. Meinhold, C. Anderson, R. Proksch, *Review of Scientific Instruments* **2016**, *87*, 073705.

[4]   M. J. Higgins, R. Proksch, J. E. Sader, M. Polcik, S. Mc Endoo, J. P. Cleveland, S. P. Jarvis, *Review of Scientific Instruments* **2006**, *77*, 013701

[5]   N. Mullin, J. K. Hobbs, *Review of Scientific Instruments* **2014**, *85*, 113703.

[6]   J. E. Sader, J. Chon, P. Mulvaney, *Review of Scientific Instruments* **1999**, *70*, 3967-3969

[7]   C. P. Green, H. Lioe, J. P. Cleveland, R. Proksch, P. Mulvaney, J. E. Sader, *Review of Scientific Instruments* **2004**, *75*, 1988-1996.

[8]   R. J. Cannara, M. Eglin, R. W. Carpick, *Review of Scientific Instruments* **2006**, *77*, 053701.

[9]   R. Garcia, E. T. Herruzo, *Nature Nanotechnology* **2012**, *7*, 217-226.

[10]   N. Sasaki, M. Tsukada, *Physical Review B* **1995**, *52*, 8471-8482

[11]   H. S. Wong, C. Durkan, N. Chandrasekhar, *ACS Nano* **2009**, *3*, 3455-3462

[12]   H. S. Wong, C. Durkan, *Nanotechnology* **2012**, *23*, 185703.

[13]   P. Xu, Y. Yang, S. D. Barber, J. K. Schoelz, D. Qi, M. L. Ackerman, L. Bellaiche, P. M. Thibado, *Carbon* **2012**, *50*, 4633-4639.

[14]   S. Kawai, T. Glatzel, S. Koch, B. Such, A. Baratoff, E. Meyer, *Physical Review B* **2009**, *80*, 085422.

[15]   S. E. Yalcin, B. A. Legg, M. Yeşilbaş, N. S. Malvankar, J.-F. Boily, *Science Advances* **2020**, *6*, eaaz9708.

[16]   A. U. Alam, M. M. R. Howlader, M. J. Deen, *Journal of Micromechanics and Microengineering* **2014**, *24*, 035010

[17]   T. Ondarcuhu, V. Thomas, M. Nunez, E. Dujardin, A. Rahman, C. T. Black, A. Checco, *Scientific Reports* **2016**, *6*, 24237.

[18]   B. A. Krajina, L. S. Kocherlakota, R. M. Overney, *Journal of Chemical Physics* **2014**, *141*, 164707.

[19]   S. Kawai, H. Kawakatsu, *Physical Review B* **2009**, *79*, 115440.

[20]   J. E. Sader, S. P. Jarvis, *Physical Review B* **2004**, *70*, 012303.

[21]   E. T. Herruzo, R. Garcia, *Beilstein Journal of Nanotechnology* **2012**, *3*, 198-206.

[22]   F. J. Giessibl, *Physical Review B* **1997**, *56*, 16010-16015.

[23] S. Kawai, T. Glatzel, S. Koch, B. Such, A. Baratoff, E. Meyer, *Physical Review B* **2010**, *81*, 085420.

[24] F. J. Giessibl, *Applied Physics Letters* **2000**, *78*, 123-125

[25] T. Seeholzer, O. Gretz, F. J. Giessibl, A. J. Weymouth, *New Journal of Physics* **2019**, *21*, 083007.